

location of the heart using information obtained from the locations of targets on the chest.

Our system intended to correct global movement during dynamic scans. It was expected that the system would work on transmission and emission data smoothed temporally and spatially. Attenuation correction artefacts due to respiration was out of the scope for our system, which were investigated in the X-ray combined PET system studies [25, 26].

Conclusion

Our technique using an optical motion-tracking device provided the reasonable information for correcting the global movement of the subject. It was shown that this system was applicable to detect and correct subject movement in cardiac PET studies at rest. We conclude that the present technique would contribute to improvement in the quantification of MBF in ^{15}O -water PET studies.

Acknowledgments This study was supported by a grant from New Energy and Industrial Technology Development Organization (NEDO) of Japan, the Budget for Nuclear Research of the Ministry of Education, Culture, Sports, Science and Technology (MEXT) of Japan, the Program for Promotion of Fundamental Studies in Health Science of the Organization for Pharmaceutical Safety and Research of Japan, Health Science Research Grant from the Ministry of Health, Labour and Welfare of Japan, a Grant-in-Aid for Young Scientists of the MEXT (B) (19700397) of Japan, and also a research grant for Advanced Medical Technology from the Ministry of Health, Labour and Welfare (MHLW) of Japan.

References

- Menke M, Atkins MS, Buckley KR. Compensation methods for head motion detected during PET imaging. *IEEE Trans Nucl Sci.* 1996;43:310–7.
- Picard Y, Thompson CJ. Motion correction of PET images using multiple acquisition frames. *IEEE Trans Med Imaging.* 1997;16:137–44.
- Lopresti BJ, Russo A, Jones WF, Fisher T, Crouch D, Altenburger DE, et al. Implementation and performance of an optical motion tracking system for high resolution brain PET imaging. *IEEE Trans Nucl Sci.* 1999;46:2059–67.
- Watabe H, Sato N, Kondoh Y, Fulton RR, Iida H. Correction of head movement using optical motion tracking system during PET study with rhesus monkey. In: *Brain Imaging Using PET*. San Diego: Academic Press; 2002. p. 1–8.
- Fulton RR, Meikle SR, Eberl S, Pfeiffer J, Constable CJ. Correction for head movements in positron emission tomography using an optical motion-tracking system. *IEEE Trans Nucl Sci.* 2002;49:116–23.
- Bloomfield PM, Spinks TJ, Reed J, Schnorr L, Westrip AM, Livieratos L, et al. The design and implementation of a motion correction scheme for neurological PET. *Phys Med Biol.* 2003;48:959–78.
- Woo SK, Watabe H, Yong C, Kim KM, Choon C, Bloomfield PM, et al. Sinogram-based motion correction of PET images using optical motion tracking system and list-mode data acquisition. *IEEE Trans Nucl Sci.* 2004;51:782–8.
- McCord ME, Bacharach SL, Bonow RO, Dilisizian V, Cuocolo A, Freedman N. Misalignment between PET transmission and emission scans: its effect on myocardial imaging. *J Nucl Med.* 1992;33:1209–14.
- Germano G, Chua T, Kavanagh PB, Kiat H, Berman DS. Detection and correction of patient motion in dynamic and static myocardial SPECT using a multi-detector camera. *J Nucl Med.* 1993;34:1349–55.
- Cooper JA, Neumann PH, McCandless BK. Detection of patient motion during tomographic myocardial perfusion imaging. *J Nucl Med.* 1993;34:1341–8.
- Bacharach SL, Douglas MA, Carson RE, Kalkowski PJ, Freedman NM, Perrone-Filardi P, et al. Three-dimensional registration of cardiac positron emission tomography attenuation scans. *J Nucl Med.* 1993;34:311–21.
- Iida H, Kanno I, Takahashi A, Miura S, Murakami M, Takahashi K, et al. Measurement of absolute myocardial blood flow with H_2^{15}O and dynamic positron-emission tomography. Strategy for quantification in relation to the partial-volume effect. *Circulation* 1988;78:104–15 (erratum in: *Circulation* 1988;78:1078).
- Iida H, Rhodes CG, de Silva R, Yamamoto Y, Araujo LI, Maseri A, et al. Myocardial tissue fraction—correction for partial volume effects and measure of tissue viability. *J Nucl Med.* 1991;32:2169–75.
- Knaepen P, Boellaard R, Götte MJ, van der Weerd AP, Visser CA, Lammertsma AA, et al. The perfusable tissue index: a marker of myocardial viability. *J Nucl Cardiol.* 2003;10:684–91.
- de Silva R, Yamamoto Y, Rhodes CG, Iida H, Nihoyannopoulos P, Davies GJ, et al. Preoperative prediction of the outcome of coronary revascularization using positron emission tomography. *Circulation.* 1992;86:1738–42.
- Knaepen P, Boellaard R, Götte MJ, Dijkman PA, van Campen LM, de Cock CC, et al. Perfusible tissue index as a potential marker of fibrosis in patients with idiopathic dilated cardiomyopathy. *J Nucl Med.* 2004;45:1299–304.
- Chareonthaitawee P, Kaufmann PA, Rimoldi O, Camici PG. Heterogeneity of resting and hyperemic myocardial blood flow in healthy humans. *Cardiovasc Res.* 2001;50:151–61.
- Yamamoto Y, de Silva R, Rhodes CG, Araujo LI, Iida H, Rechavia E, et al. A new strategy for the assessment of viable myocardium and regional myocardial blood flow using ^{15}O -water and dynamic positron emission tomography. *Circulation.* 1992;86:167–78.
- Iida H, Rhodes CG, de Silva R, Araujo LI, Bloomfield PM, Lammertsma AA, et al. Use of the left ventricular time-activity curve as a noninvasive input function in dynamic oxygen- 15 -water positron emission tomography. *J Nucl Med.* 1992;33:1669–77.
- Naum A, Laaksonen MS, Tuunainen H, Oikonen V, Teräs M, Kempainen J, et al. Motion detection and correction for dynamic (^{15}O -water myocardial perfusion PET studies. *Eur J Nucl Med Mol Imaging.* 2005;32:1378–83.
- Iida H, Miura S, Kanno I, Ogawa T, Uemura K. A new PET camera for noninvasive quantitation of physiological functional parametric images: HEADTOME-V-Dual. In: *Quantification of brain function using PET*. San Diego: Academic Press; 1996. 57–61.
- Wienhard K, Dahlbom M, Eriksson L, Michel C, Bruckbauer T, Pietrzyk U, et al. The ECAT EXACT HR: performance of a new high resolution positron scanner. *J Comput Assist Tomogr.* 1994;18:110–8.

23. Iida H, Rhodes CG, Araujo LI, Yamamoto Y, de Silva R, Maseri A, et al. Noninvasive quantification of regional myocardial metabolic rate for oxygen by use of $^{18}\text{O}_2$ inhalation and positron emission tomography. Theory, error analysis, and application in humans. *Circulation*. 1996;94:792–807.
24. Juslin A, Lötjönen J, Nesterov SV, Kalliokoski K, Knuuti J, Ruotsalainen U. Alignment of 3-dimensional cardiac structures in O-15-labeled water PET emission images with mutual information. *J Nucl Cardiol*. 2007;1:82–91.
25. McQuaid SJ, Hutton BF. Sources of attenuation-correction artefacts in cardiac PET/CT and SPECT/CT. *Eur J Nucl Med Mol Imaging*. 2008;35:1117–23.
26. Gould KL, Pan T, Lohin C, Johnson NP, Guha A, Sdringola S. Frequent diagnostic errors in cardiac PET/CT due to misregistration of CT attenuation and emission PET images: a definitive analysis of causes, consequences, and corrections. *J Nucl Med*. 2007;48:1112–21.

Impaired Myocardium Regeneration With Skeletal Cell Sheets—A Preclinical Trial for Tissue-Engineered Regeneration Therapy

Shigeru Miyagawa,¹ Atsuhiko Saito,² Taichi Sakaguchi,¹ Yasushi Yoshikawa,¹ Takashi Yamauchi,¹ Yukiko Imanishi,¹ Naomasa Kawaguchi,³ Noboru Teramoto,⁴ Nariaki Matsuura,³ Hidehiro Iida,⁴ Tatsuya Shimizu,⁵ Teruo Okano,⁵ and Yoshiki Sawa^{1,6}

Background. We hypothesized that autologous skeletal cell (SC) sheets regenerate the infarct myocardium in porcine heart as a preclinical trial.

Methods and Results. The impaired heart was created by implantation of ameroid constrictor on left anterior descending for 4 weeks. SCs isolated from leg muscle were cultured and detached from the temperature-responsive domain-coated dishes as single monolayer cell sheet at 20°C. The following therapies were conducted: SC sheets (SC group, n=5); sham (C group n=5). Echocardiography demonstrated that cardiac performance was significantly improved in the SC group 3 and 6 months after operation (fractional area shortening, 3 months; SC vs. C=49.5±2.8 vs. 24.6±2.0%, P<0.05) and left ventricle dilatation was well attenuated in the SC group. Color kinesis index showed that distressed regional diastolic and systolic function in infarcted anterior wall was significantly recovered (SC vs. C=57.4±8.6 vs. 30.2±4.7%, P<0.05, diastolic: 58.5±4.5 vs. 35.4±6.6%, P<0.05, systolic). Factor VIII immunostains demonstrated that vascular density was significantly higher in the SC group than the C group. And % fibrosis and cell diameter were significantly lower in the SC group. And hematoxylin-eosin staining depicted that skeletal origin cells and well-developed-layered smooth muscle cells were detected in the implanted area. Positron emission tomography showed better myocardial perfusion and more viable myocardial tissue in the distressed myocardium receiving SC sheets compared with the myocardium receiving no sheets.

Conclusions. SC sheet implantation improved cardiac function by attenuating the cardiac remodeling in the porcine ischemic myocardium, suggesting a promising strategy for myocardial regeneration therapy in the impaired myocardium.

Keywords: Cells, Heart failure, Myocardial infarction, Tissue, Transplantation.

(*Transplantation* 2010;90: 364–372)

Despite the recent remarkable progress in medical and surgical treatments for heart failure, end-stage heart failure has been still a major cause of death worldwide. After myocardial infarction, the myocardium is capable of a limited regenerative capacity and no medication or procedure used clinically has shown efficacy in regenerating myocardial scar

tissue with functioning tissue. Thus, there is a need for new therapeutics to regenerate damaged myocardium.

Recent developments in tissue engineering show promise for the creation of functional cardiac tissues without the need for biodegradable alternatives for the extracellular matrix (1). And we reported that cardiomyocyte sheets have been developed by using temperature-responsive culture dishes and these sheets survived in the back of nude rats and showed a spontaneous contraction over a long period of time (2). Recent reports suggested that cardiomyocyte sheets integrated with the impaired myocardium and improved cardiac performance in a rat model of ischemic myocardium (3).

This work was supported by a Grant-in-Aid for Scientific Research in Japan.

¹ Division of Cardiovascular Surgery, Department of Surgery, Faculty of Medicine, Osaka University Graduate School of Medicine, Suita, Osaka, Japan.

² Medical Center for Translational Research, Osaka University Hospital, Osaka, Japan.

³ Department of Pathology, School of Allied Health Science, Faculty of Medicine, Osaka University Graduate School of Medicine, Suita, Osaka, Japan.

⁴ Department of Investigative Radiology, National Cardiovascular Center Research Institute, Tokyo, Japan.

⁵ Tokyo Women's Medical University Institute of Advanced Biomedical Engineering and Science, Tokyo, Japan.

⁶ Address correspondence to: Yoshiki Sawa, M.D., Department of Cardiovascular Surgery, Osaka University Graduate School of Medicine, 2-2 Yamada-oka, Suita, Osaka 565-0871, Japan.

E-mail: sawa@surg1.med.osaka-u.ac.jp

S.M. participated in the writing of the paper; A.S. participated in research design; T.S. and Y.Y. participated in data analysis; T.Y., Y.I., N.K., and N.T. participated in the performance of research; N.M., H.I., T.S., T.O., and Y.S. participated in research design.

Received 15 December 2009. Revision requested 2 January 2010.

Accepted 6 May 2010.

Copyright © 2010 by Lippincott Williams & Wilkins

ISSN 0041-1337/10/9004-364

DOI: 10.1097/TP.0b013e3181e6f201

And more recently, in the aim of clinical application, nonligature implantation of skeletal myoblast sheet regenerated the damaged myocardium and improved global cardiac function by attenuating the cardiac remodeling in the rat ligation model (4) and dilated cardiomyopathy hamster model (5). This cell delivery system by using cell sheets implantation showed better restoration of damaged myocardium compared with needle injection (4, 5). Moreover, grafting of skeletal myoblast sheets attenuated cardiac remodeling and improved cardiac performance in pacing-induced canine heart failure model (6).

Given this body of evidence, we hypothesized that the autologous skeletal cell (SC) sheet implantation might remodel the chronic heart failure caused by ischemic injury.

Therefore, this preclinical study using Swine model was designed to test therapeutic effectiveness.

MATERIALS AND METHODS

Myocardial Infarction Model

"Principles of Laboratory Animal Care" formulated by the National Society for Medical Research and the "Guide for the Care and Use of Laboratory Animals" prepared by the Institute of Laboratory Animal Resource and published by the National Institutes of Health (NIH Publication No. 86-23, revised 1985). This animal experiment was approved by the Animal Care Committee of Osaka university graduate school of medicine. We induced acute myocardial infarction of 10 swine (20 kg, KEARI, Japan) by the following method. Swine were preanesthetized by intramuscular injection of ketamine hydrochloride 20 mg/kg (Ketalar, Sankyo, Japan) and xylazine 2 mg/kg (Seractar, Bayer). Animals were positioned spine and a 22-gauge indwelling needle (Surflo F&F, Terumo, Tokyo, Japan) was inserted in the central vein of the auricle. A three-way cock (Terufusion TS-TR2K, Terumo, Tokyo, Japan) was attached to the external cylinder of the indwelling needle, and an extension tube was connected for continuous anesthetic injection. The animals were intubated with an endotracheal cannula (6 Fr, Sheridan) using a pharyngoscope and then connected to an artificial respirator (Harvard, USA) by the cannula. Artificial respiration was implemented at a stroke volume of 200 to 300 mL/stroke and a stroke frequency of 20/min. The animals were continuously drip injected with propofol 6 mg/kg/hr (Diprivan, AstraZeneca) and vecuronium bromide 0.05 mg/kg/hr (Musculux, Sankyo Yell Yakuhin Co., Ltd., Japan) using a syringe pump (Terufusion TE-3310N, Terumo, Japan). The animal was then fixed in a recumbent position, so that the left thorax was exposed, and the outer layer of skin and muscles between the third and fourth ribs were dissected. After confirming the cutting into the thoracic cavity, the distance between the third and fourth ribs was widened with a rib spreader to allow a direct view of the left auricle and the LAD coronary artery. The pericardium was dissected along the LAD from the upper part of the left auricle (~6 cm) to expose the myocardium around the LAD. LAD on the proximal side below the left auricle from the myocardium was exfoliated for approximately 1 cm, and then a small amount of lidocaine hydrochloride jelly (Xylocaine jelly, AstraZeneca) was applied to allow for anesthetizing the area. An ameroid constrictor (COR-2.50-SS, Research Instruments) was then fit using No. 1 or 2 suture. The chest cavity was closed to end the procedures. The animals were randomly divided into two treatment groups: the first received autologous SC sheet implantation (SC group, n=5). For control, we have performed sham operation (C group, n=5).

Preparation of Skeletal Cell Sheets for Grafting

One week after implantation of ameroid constrictor on LAD, skeletal muscle weighing approximately 5 g was removed from the pretibial region with the porcine under general anesthesia. Following the addition of trypsin-ethylenediaminetetraacetic acid (Gibco, Grand Island, NY), excessive connective tissue was carefully removed to minimize the content of contaminating fibroblasts, and the muscle tissue was minced until the

fine pieces formed a homogeneous mass. The specimens were then incubated at 37°C in shaker bath with 0.5% type 1 collagenase (Gibco) in Dulbecco's modified Eagle's medium (Gibco). After brief placement, the fluid was collected, and the same volume of culture medium, SkBM (Cambrex, Walkersville, MD) supplemented with fetal bovine serum (Thermo Trace, Melbourne, Australia), was added to halt the enzymatic digestion process. The cells were collected by centrifugation, and the putative SCs were seeded into 150 cm² polystyrene flasks after removal of fibroblasts by sedimentation for a few hours and cultured in SkBM at 37°C. During the culture process, we maintained cell densities at less than 70% confluence by carrying out passaging of cells for one time to prevent SCs from premature differentiation and fusion process resulting in myotubes formation. When the cells became approximately 70% confluent after 10 to 11 days cultivation, the cells were dissociated from the flasks with trypsin-ethylenediaminetetraacetic acid and reincubated on 100 mm temperature-responsive culture dishes (Cellseed, Tokyo, Japan) at 37°C with the cell numbers adjusted to 1×10^7 per dish. More than 90% of these cells were desmin positive (Fig. 1). After 4 days, the dishes were removed to refrigerator set at 20°C, and left there for approximately 30 min. During that time, the SC sheets detached spontaneously from the surfaces. Each sheet had a diameter of 30 to 40 mm and consisted of layers of SCs; the sheets were approximately 100- μ m thick in cross-sectional views (Fig. 1). Approximately 10 sheets were obtained from the 5 g of skeletal muscle.

Implantation of Skeletal Cell Sheets

Autologous SC sheet implantation was performed in the swine 4 weeks after LAD ligation. Swine were anesthetized as mentioned above. The swine were exposed through the sternum. The infarct area was identified visually on the basis of surface scarring and abnormal wall motion. In the SC group, we implanted 10 SC sheets into the infarcted myocardium. The control group was treated similarly but received no SC sheets. Because pilling up four or more sheets caused the central necrosis of the myoblasts presumably because the lack of in oxygen supply, we decided to pile two or three layers of the SC sheet over the broad surface of the impaired heart.

Measurement of Cardiac Function

Swine were anesthetized as mentioned above. Cardiac ultrasonography was performed with a commercially available echocardiograph, SONOS 5500 (PHILIPS Electronics, Tokyo, Japan). A 3-MHz annular array transducer was placed on a layer of acoustic coupling gel that was applied to the left hemithorax. Swine were examined in a shallow left lateral decubitus position. The heart was first imaged in the two-dimensional mode in short-axis views at the level of the largest left ventricle (LV) diameter. The calculation of the LV volume was based on the LV short-axis area using AQ system (7). And fractional area shortening (FAS) of the LV diastolic was calculated as follows:

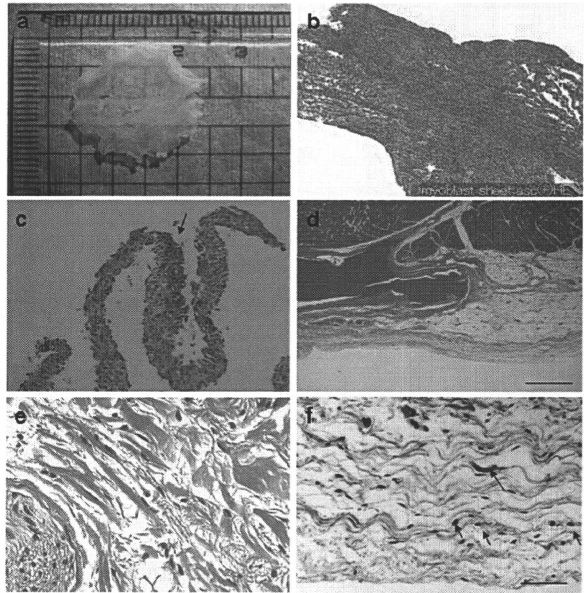
$$\text{FAS (\%)} = \left[\frac{\text{LV end-diastolic area} - \text{LV end-systolic area (ESA)}}{\text{LV end-diastolic area}} \right] \times 100$$

These data are presented as the average of measurements of two or three selected beats.

Quantification of Regional Diastolic and Systolic Function by Color Kinesis

Diastolic CK images were obtained using a commercially available ultrasound system (SONOS 5500, Philips Medical Systems) from the LV midpapillary short-axis view for the determination of wall motion asynchrony as previously reported (8). CK examined every image pixel within the region of interest, which was drawn around the LV cavity, classifying it as blood or tissue based on integrated backscatter data. During diastole, each pixel was tracked into the next frame, and pixel transitions from endocardium to blood were detected and interpreted as diastolic endocardial motions. These pixel transitions were encoded using a color hue specific to each consecutive video frame, so that each color represents the excursion of that segment during a 33-ms period of time. The sites of regional LV diastolic wall motion or regions of interest were set on the basis of standard segmentation models: anterior, lateral, posterior, inferior, anteroseptal wall. The CK diastolic index was defined as the LV segmental filling fraction

FIGURE 1. Histological characteristics of skeletal cell (SC) sheet. (a) SC sheet detached from the Poly (*N*-isopropylacrylamide)-grafted polystyrene by lowering the temperature. Its size is approximately 3 cm × 2 cm². (b) Hematoxylin-eosin (H&E) stain; cross-sectional views of SC sheet in vitro. SC sheet demonstrates homogeneous heart-like tissue. (c) Not so many smooth muscle cells were detected in the SC sheets. The arrow indicates the smooth muscle cells in the SC sheet. (d) H&E stain revealed that SC sheets attached on the surface of epicardium. Left square bracket indicates implanted SC sheets. (e) Oval-shaped cells that showed positive for eosin in cytoplasm were detected in the SC group microscopically in some layers over epicardium. (f) Elastic Masson Goldner showed that oval-shaped cells that supposed to origin from skeletal tissue exist in the transplantation site. Arrows indicate oval-shaped cells that suppose to be originated from skeletal tissue.



during the first 30% of the diastolic filling time (LV segmental cavity area expansion during the first 30% of diastole, divided by the segmental end-diastolic LV cavity area expansion, expressed as a percentage). We introduced the use of color kinesis method that displays endocardial motion in real time to evaluate the regional systolic function (8).

Histopathology

LV myocardium specimens were obtained 6 months after the SC sheet implantation. Each specimen was fixed with 10% buffered formalin and embedded in paraffin. A few serial sections were prepared from each specimen and stained with hematoxylin-eosin (H&E) stain and elastica Masson-Goldner for histological examination or with Masson's trichrome stain to assess the collagen content.

To label vascular endothelial cells so that the blood vessels could be counted, immunohistochemical staining of factor VIII-related antigen was performed according to a modified protocol. Frozen sections were fixed with a 2% paraformaldehyde solution in phosphate-buffered saline (PBS) for 5 min at room temperature, immersed in methanol with 3% hydrogen peroxide for 15 min, then washed with PBS. The samples were covered with bovine serum albumin solution (DAKO LSAB Kit DAKO CORPORATION, Denmark) for 10 min to block nonspecific reactions. The specimens were incubated overnight with an Enhanced Polymer One-Step Staining (EPOS)-conjugated antibody against factor VIII-related antigen coupled with horseradish peroxidase (DAKO EPOS Anti-Human Von Wille brand Factor/HRP, DAKO, Denmark). After the samples were washed with PBS, they were immersed in diaminobenzidine solution (0.3 mg/mL diaminobenzidine in PBS) to obtain positive staining. Ten different fields at 200× magnification were randomly selected, and the number of the stained vascular endothelial cells in each field was counted under a light microscope. The result was expressed as the number of blood vessels per square millimeter.

The following antibodies against smooth muscle cells and skeletal myosin (slow) were used to evaluate the existence of SCs: primary antibodies, anti-

smooth muscle actin (clone 1A4, DAKO) antiskeletal myosin (slow) (clone NOQ7.5.4D, Sigma); secondary antibodies, anti-mouse Ig biotinylate (DAKO).

Picro-sirius red staining for the assessment of myocardial fibrosis or periodic acid-Schiff staining for that of cardiomyocyte hypertrophy was performed as described (9).

Positron Emission Tomography Procedure

We performed positron emission tomography (PET) studies on pigs which were transplanted SC sheets and control by using ¹⁵O-water and ¹⁸F-FDG. The pigs were anesthetized by the introduction of pentobarbital followed by continuous inhalation of propofol (4 mg/kg/hr) and were placed supine on the bed of the scanner. PET was performed using a HEADTOME-III tomograph (Shimadzu, Kyoto, Japan) and data were analyzed as described elsewhere (10).

Holter Electrocardiography

To evaluate arrhythmia we used Holter electrocardiography (ECG) for 24 hours. We checked arrhythmia by checking the number of ventricular premature beat after SC sheet implantation in myocardial infarction porcine (n=3).

Data Analysis

Data are expressed as means ± SEM and subjected to multiple analysis of variance (ANOVA) using the StatView 5.0 program (Abacus Concepts, Berkeley, CA). Echocardiographic data were first analyzed by two-way repeated measurement ANOVA for differences across the whole time course, and one-way ANOVA with the Tukey-Kramer posthoc test was used to verify the significant for the specific comparison at each time point. To assess the significance of the differences between individual groups concerning other numeral data, statistical evaluation was performed with an unpaired *t* test. Statistical significance was determined as having a *P* value less than 0.05.

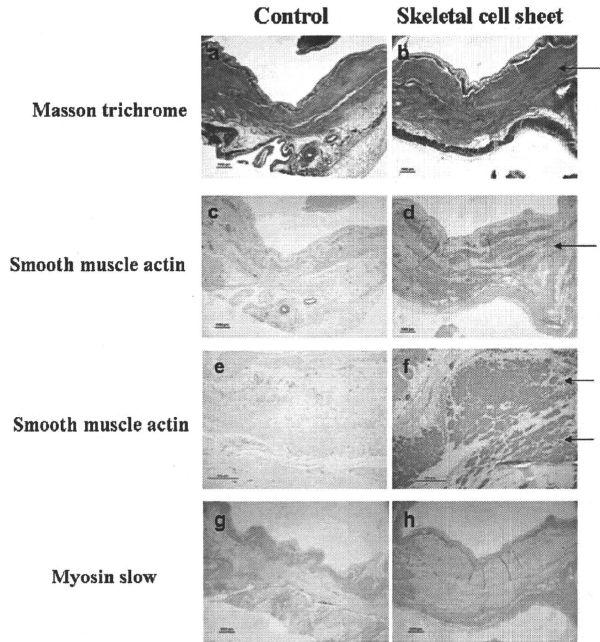


FIGURE 2. The detection of a large quantity of skeletal cells (SCs) in the center of the scar. (a and b) Masson trichrome staining reveals that some layered muscles are detected in the center of the scar in the SC sheet transplantation group, whereas not in the control. (c–f) Smooth muscle actin staining demonstrated that well-developed smooth muscle cells occupied in the center of the scar in the SC sheet transplantation group, whereas only smooth muscle cells which are formed vasculature are detected in the control. (g and h) Slow-type myosin staining showed that no positive cells exist in the center of the scar. This means that SCs which are detected in the center of the scar are not the residual myocyte after infarction.

RESULTS

Characteristics of Myoblast Sheet

We obtained monolayered myoblast sheets by lowering the temperature, which released them from the Poly(*N*-isopropylacrylamide)-grafted polystyrene. Its size is approximately $3\text{ cm} \times 2\text{ cm}^2$ (Fig. 1a). H&E staining demonstrated that SC sheet contained a lot of SCs and SC sheets had an appearance of homogeneous tissue, which thickness of one SC sheet was approximately $100\ \mu\text{m}$ (Fig. 1b). Some smooth muscle cells are detected in the SC sheets, but those cells are not majority (Fig. 1c).

Histological Assessment

H&E staining demonstrated that transplanted SC sheets were attached in the epicardium (Fig. 1d) and oval-shaped cell that showed positive for eosin in cytoplasm were detected in the SC group microscopically in some layers over epicardium (Fig. 1e). Elastic Masson-Goldner showed that oval-shaped cells that supposed to origin from skeletal tissue exist in the transplantation site (Fig. 1f). These cells were not seen in the control group. And the SC group demonstrated decrease in the cross-sectional LV area compared with the C groups (Fig. 2a). Masson's trichrome staining showed that clustered SCs were detected in the center of the scar, whereas clustered SCs were not detected in the C group (Fig. 2a, b). Many clusters of well-developed smooth muscle cells exist in the center of the whole scar in the SC group, whereas in the C

group, smooth muscle cells which formed vasculature exist in the scar (Fig. 2c–f). Although slow-type myosin-positive cells exist only on the endocardium and epicardium, those cells were not detected in the center of scar (Fig. 2g,h). So these figures depict that the skeletal muscle cells that exist in the center of the scar is not residual myocyte after infarction.

Quantification of Histopathology

In the SC group, vascular density was found to be significantly higher than in the C groups (SC vs. C = 217.1 ± 30.2 vs. 114.2 ± 18.2 /field; $P < 0.05$) (Fig. 3b).

Picro-sirius red staining demonstrated that % fibrosis was significantly reduced in the SC group compared with the C group (SC vs. C = 1.6 ± 0.2 vs. $3.1 \pm 0.3\%$; $P < 0.05$) (Fig. 3b). Periodic acid-Schiff staining showed that cell diameter was significantly shorter in the SC group than the C group (SC vs. C = 10.7 ± 0.3 vs. $18.3 \pm 1.4\ \mu\text{m}$; $P < 0.05$) (Fig. 3b).

These histological findings were universally identified in the native myocardial tissue without distinction of distance from the grafted region.

Functional Assessment of the Infarcted Myocardium

The FAS and LV end-ESA scores at baseline were not significantly different between the two groups.

Three months after the implantation, two-dimensional echocardiography showed significant improvement of the

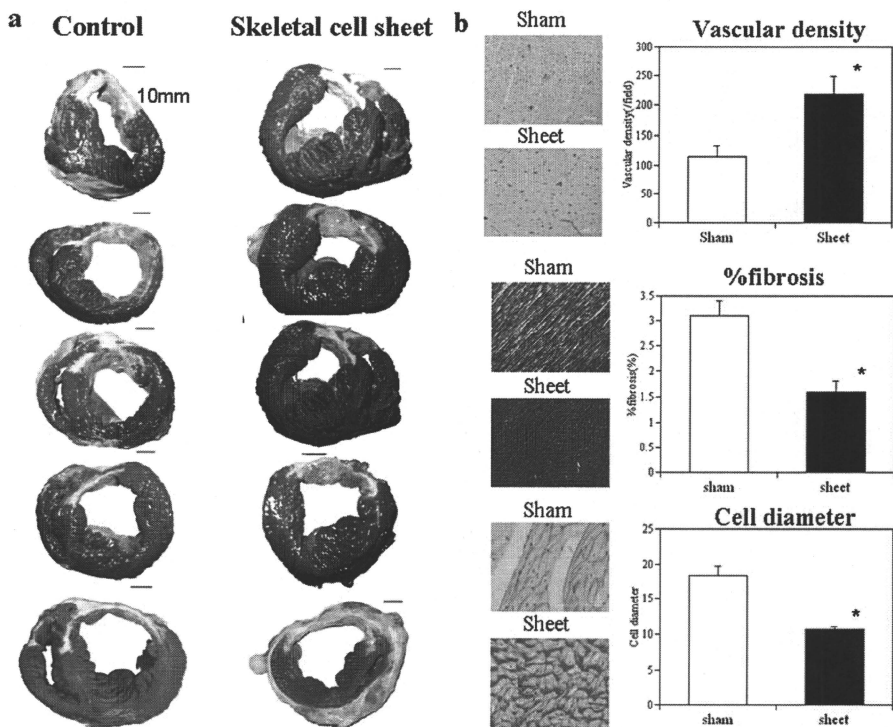
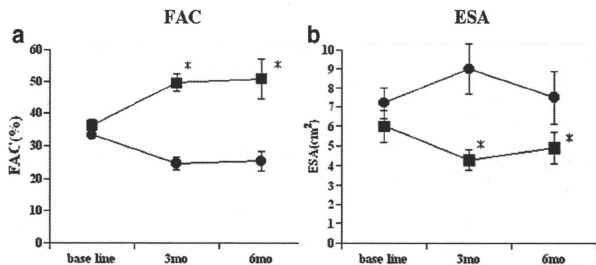


FIGURE 3. Macroscopic images of impaired myocardium receiving skeletal cell (SC) sheets and histological evaluation. (a) In the SC group, the anterior wall has recovered compared with the C group. In the SC group, the short axis area of the left ventricle (LV) is small compared with the C groups. In contrast, the C group shows a dilated LV and the anterior wall is thinner than in the SC groups. (b) Histological evaluation. Vascular density: the SC group showed a significant improvement in vascular density as assessed by immunostaining for the factor VIII-related antigen. **P* less than 0.05 vs. C. The ratio of fibrosis-occupied area (% fibrosis) at a site remote from the infarcted heart region: picro-sirius red staining demonstrated that % fibrosis at a site remote from the infarcted heart region was significantly reduced in the SC group compared with the C group. **P* less than 0.05 vs. C. The diameter of cardiomyocyte: the diameter of cardiomyocyte is significantly shorter in the SC group than the C group. **P* less than 0.05 vs. C.

FIGURE 4. Global functional effects of infarcted myocardium receiving the implant. Global systolic function assessed by the fractional shortening (FAS) (a) was significantly improved in the skeletal cell (SC) group 3 months after transplantation, and these functional improvements were preserved 6 months after SC sheet implantation. (b) The end-systolic area (ESA) was significantly smaller in the SC group than in the C groups 3 and 6 months after implantation. **P* less than 0.05 vs. C, ■: SC sheet, ●: control.



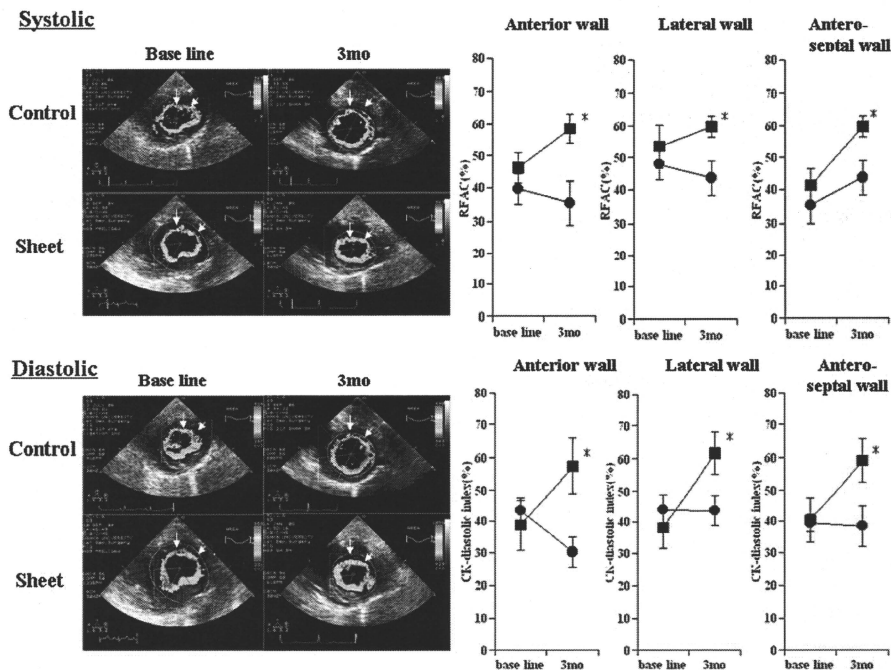


FIGURE 5. Systolic function: regional systolic function was significantly recovered in the skeletal cell (SC) group 3 months after implantation compared with the C group in the anterior, lateral, and anteroseptal wall. **P* less than 0.05. Diastolic function: regional dysfunction was significantly recovered in the SC group 3 months after implantation compared with the C group in the anterior, lateral, and anteroseptal wall. Before treatment, diastolic dysfunction was observed in the infarction area of myocardium and the regional delayed relaxation was detected in the remote site of infarction by color kinesis. But this phenomenon was disappeared after SC sheet implantation. **P* less than 0.05, ■: SC sheet, ●: control.

FAS (Fig. 4a) in the SC group compared with the C group (SC vs. C=49.5±2.8 vs. 24.6±2.0%, *P*<0.05). These functional improvements were preserved 6 months after implantation (SC vs. C=50.8±6.4 vs. 25.3±2.8%, *P*<0.05). The ESA was significantly smaller in the SC group than in the C group 3 months after the implantation (SC vs. C=4.3±0.5 vs. 9±1.3 cm², *P*<0.05) (Fig. 4b). These attenuation of LV dilatation were preserved 6 months after implantation (SC vs. C=4.9±0.8 vs. 7.5±1.4 cm², *P*<0.05). During this long-term observation, all SC sheet-treated animals were alive and exhibited no malignant arrhythmia assessed by 24-hour Holter ECG once a week (data not shown).

Before treatment, diastolic dysfunction was observed in the infarction area of myocardium and the regional delayed relaxation was detected in the remote site of infarction by color kinesis. After 3 months after implantation, CK-diastolic index in the lateral (SC vs. C=61.7±6.4 vs. 43.7±4.8%, *P*<0.05), anterior (SC vs. C=57.4±8.6 vs. 30.2±4.7%, *P*<0.05), and anteroseptal (SC vs. C=59±6.6 vs. 38.4±6.6%, *P*<0.05) segment were significantly ameliorated

in the SC group compared with the C group, and regional systolic function in transplanted site was significantly improved in the SC group while not in the C groups (SC vs. C: lateral, 59.8±3.3 vs. 43.6±5.4%, *P*<0.05; anterior, 58.5±4.5 vs. 35.4±6.6%, *P*<0.05; anteroseptal, 59.8±3.3 vs. 43.6±5.4%, *P*<0.05), respectively (Fig. 5).

We could detect no ventricular premature beat for 24 hr by the Holter ECG in three myocardial infarction porcine received SC sheets.

Regional Myocardial Blood Flow and Residual Myocardial Tissue

PET study by using ¹⁵O-water showed that the myocardial water-perfusible tissue fraction and myocardial blood flow were higher in the anterior wall where SC sheets were implanted compared with the myocardium receiving no sheets. These data depict that myocardial blood flow was better and microcirculation in the infarcted myocardium was preserved in the SC sheets implanted myocardium. PET study by using ¹⁸F-FDG revealed that more viable myocardial tis-

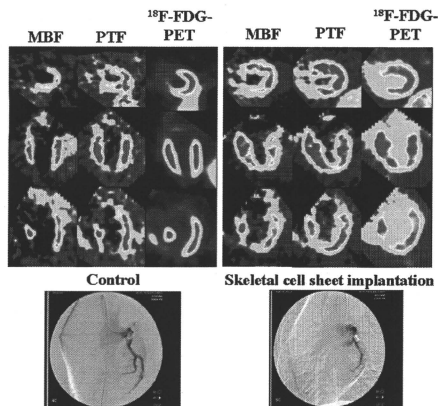


FIGURE 6. Positron emission tomography (PET) study revealed that perfusable tissue fraction (PTF) and myocardial blood flow (MBF) were higher and more viable myocardial tissues were preserved in the skeletal cell sheets implanted site compared with the myocardium receiving no sheets.

sues were preserved in the skeletal sheet implanted myocardium compared with the myocardium receiving no sheets. Coronary angiography revealed that LAD was occluded by the ameroid constrictor in both cases (Fig. 6).

DISCUSSION

Over the past several years, increasing awareness of the shortcomings of heart transplantation and left ventricular assist system implantation has led cardiovascular surgeons to consider alternative means of treating end-stage heart failure. In clinical setting, cellular cardiomyoplasty has been reported to have the potential of fundamental regenerative capability and has already been introduced in clinical trials with skeletal myoblast (11) or bone marrow mononuclear cells (12), and results suggest that it is a relatively feasible and safety therapy as a therapeutic angiogenesis. In this setting, cardiac tissue implantation was proposed to the treatment of end-staged heart failure as a new concept of regenerative therapy and experimentally some groups depicted it's effectiveness in the damaged myocardium (13, 14). We also reported that cell sheets have great impacts on restoration of damaged myocardium in the rat infarction model (3, 4) and dilated cardiomyopathy hamster (5). To convince the effectiveness of cell sheets in preclinical trial, we examined whether autologous SC sheets implantation might become one of the armamentarium of regenerative therapy for chronic heart failure caused by myocardial infarction in the porcine model.

The potential added advantages of the cell sheet implantation method include the implantation of a high number of cells with minimum cell loss. In contrast, the injection method is associated with a high loss of cells or surface proteins due to the trypsin treatment. Despite a high number of cell loss in needle injection, the cell sheet implantation

method might provide the advantages of a higher number of cell implantation without cellular community destruction, leading the more improvement of cardiac performance rather than cell injection method (4). In case of needle injection, inflammation accompanied with destruction of myocardium induced by needle injection promotes graft death after cell transplantation (15).

To examine the effects of the SC sheet implantation therapy, we analyzed cardiac function and performed a histological assessment of the infarcted heart after SC sheet transplantation in a swine infarction model. SC sheet implantation therapy significantly induced angiogenesis, reduction of fibrosis histologically. And cell diameter of host myocyte was significantly attenuated its hypertrophy compared with the no treatment group. PET study revealed the better regional blood perfusion and better regional myocardial viability in the myocardium receiving cell sheets compared with the myocardium receiving no sheets.

Moreover, SC sheet implantation induced functional recovery of damaged myocardium. Especially, we demonstrated that the regional diastolic and systolic dysfunction was well recovered in the sheet implanted group. Before treatment, diastolic dysfunction of infarcted area and regional delayed relaxation of noninfarcted site were detected by color kinesis in the porcine infarcted myocardium. After treatment, diastolic dysfunction of infarcted site was significantly recovered and the phenomenon of regional delayed relaxation in noninfarcted site was not seen. Presumably, implanted elastic myoblast sheets and a large quantity of well-developed smooth muscle cells, which are detected in the center of the scar, improved the regional diastolic dysfunction of implanted site. Although SC sheet can not contract *in vivo* after implantation, this recovery of diastolic disassociation of LV might result in the recovery of systolic dysfunction.

To the best of our knowledge, this is the first report in which tissue-engineered SC sheets implantation was successfully used to improve cardiac performance in a large animal model of ischemic myocardium according to the Laplace's theory.

The mechanisms of the restoration of damaged myocardium by SC sheet implantation might be complicated and many pathways might affect the recovery of ischemic myocardium. Recent reports depict that cell sheets enhance the recruitment of hematopoietic stem cells through the release of stromal-derived factor 1 (4). The fact of thicker anterior wall and the improvement of regional function might depend on both the recruitment of cytokine releasing stem cells, survival of grafted cells, and well-developed smooth muscle cells. And these cells might have good elasticity and these elastic cells and tissues softened the stiffness of anterior wall in association with the attenuating fibrosis even in the infarct area. This reduced stiffness of anterior wall might lead to the improvement of the diastolic dysfunction. Transplanted SCs cannot differentiate into cardiomyocyte anymore, but regional systolic function improved in the transplanted site. Probably, the improvement of regional diastolic function due to elastic cells might be responsible for the restoration of regional systolic dysfunction. Recent reports demonstrated that regional left ventricular myocardial relaxation was closely related to regional myocardial contraction (16) and the improvement of regional myocardial relaxation leads to the

recovery of global diastolic function (17). Moreover, the improvement of regional systolic function is closely related to global systolic function (18). We assume that this theory about the relationship between diastolic and systolic function is one of the mechanisms about the improvement of diastolic and systolic function in the cell sheet transplanted myocardium.

Question is why the well-developed smooth muscle cells exist in the center of the scar in the SC sheet group after transplantation despite a small quantity of smooth muscle cells in the SC sheet? Does a small quantity of smooth muscle cells in the SC sheet proliferate after transplantation? Do progenitor cells in the SC sheet differentiate to smooth muscle cells? Do progenitor cells or smooth muscle cells in the host myocardium migrate to the implanted site and proliferate? To the regret, there is no data to answer these questions exactly in this article and more detailed studies are needed to elucidate this important question.

Some reports depicted that the expression of hepatocyte growth factor (HGF) in the myoblast sheet transplanted ischemic myocardium is higher compared with the nontransplanted ischemic myocardium (4). HGF has an antifibrotic activity both through the activation of a matrix degradation pathway (19), restoration of cytoskeletal proteins on cardiomyocyte (20), and induce angiogenesis in the ischemic myocardium (21). Our study demonstrated that % fibrosis was significantly reduced in the SC sheet transplanted group. This paracrine secretion of HGF from SC sheets might attribute the reduction of % fibrosis. In our study, much more factor VIII-positive cells are detected in the SC sheet transplanted myocardium. This might be induced by paracrine secretion of HGF and angiogenesis might rescue the ischemic host cardiomyocyte and bring about the improvement of the distressed function of host cardiomyocyte. The distressed cytoskeletal proteins on the cardiomyocyte in the ischemic myocardium might be reorganized by the HGF secreted from skeletal sheet and the restoration of cytoskeletal proteins might lead to the improvement of cardiac function. And some reports demonstrated that myoblast sheets maintain the distressed cytoskeletal proteins on the host cardiomyocyte in the dilated cardiomyopathy hamster model (5). Consequently, cell sheet treatment is appropriate for recovery of ischemic cardiomyopathy. Recent research works demonstrated that several regenerative factors such as insulin-like growth factor-1 (22) and Thymosin b4 (23) were expressed in the rat ischemic myocardium model after myoblast sheet implantation by reverse-transcriptase polymerase chain reaction analysis (data not shown). After myoblast sheet transplantation to ischemic myocardium, several regenerative factors are expressed in the transplanted site, and these long-term and low-dosed expressed regenerative factors might cooperatively restore the damaged myocardium.

We could find no ventricular premature beat analyzed by Holter ECG after SC sheet implantation. We have already proved that in the rat infarction model, arrhythmia is less in the SC sheet implantation group compared with the needle injection group and this work represented that more monocyte chemoattractant protein-1-positive cells and CD11b (macrophage marker)-positive cells were detected in the needle injection group compared with SC sheet implantation (data

not shown). We speculate that needles destroy the myocardium and this destroyed myocardium may induce the inflammation and this inflammation may induce the arrhythmia. Conversely, SC sheet implantation technique normally does not destroy the myocardium when they are implanted to recipient heart. Moreover, SC sheet will survive on the epicardium and electrical wave originated from implanted myoblasts may not deliver to the recipient myocardium directly. But when we implant myoblasts by needle injection, implanted myoblasts survive in the center of the myocardium and electrical wave will deliver to the myocardium directly, leading to the arrhythmia.

In conclusion, we have preclinically demonstrated SC sheets produced histologically and functionally apparent prevented the deterioration of the impaired myocardium in the swine model. These data provide a basis for attempting clinical cell sheet implantation in ischemic disease as the armamentarium to promote the regeneration of chronic heart failure caused by myocardial infarction.

ACKNOWLEDGMENTS

The authors thank Shigeru Matsumi and Masako Yokoyama for their excellent technical assistance.

REFERENCES

- Shimizu T, Yamato M, Akutsu T, et al. Fabrication of pulsatile cardiac tissue grafts using a novel 3-dimensional cell sheet manipulation technique and temperature-responsive cell culture surfaces. *Circ Res* 2002; 90: e40.
- Shimizu T, Sekine H, Isoi Y, et al. Long-term survival and growth of pulsatile myocardial tissue grafts engineered by the layering of cardiomyocyte sheets. *Tissue Eng* 2006; 12: 499.
- Miyagawa S, Sawa Y, Sakakida S, et al. Tissue cardiomyoplasty using bioengineered contractile cardiomyocyte sheets to repair damaged myocardium: Their integration with recipient myocardium. *Transplantation* 2005; 80: 1586.
- Memon IA, Sawa Y, Fukushima N, et al. Repair of impaired myocardium by means of implantation of engineered autologous myoblast sheets. *J Thorac Cardiovasc Surg* 2005; 130: 1333.
- Kondoh H, Sawa Y, Miyagawa S, et al. Longer preservation of cardiac performance by sheet-shaped myoblast implantation in dilated cardiomyopathic hamsters. *Cardiovasc Res* 2006; 69: 466.
- Hata H, Matsumiya G, Miyagawa S, et al. Grafted skeletal myoblast sheets attenuate myocardial remodeling in pacing-induced canine heart failure model. *J Thorac Cardiovasc Surg* 2006; 132: 918.
- Mor-Avi V, Vignon P, Bales AC, et al. Acoustic quantification indexes of left ventricular size and function: Effects of signal averaging. *J Am Soc Echocardiogr* 1998; 11: 792.
- Ishii K, Miwa K, Makita T, et al. Prolonged posts ischemic regional left ventricular delayed relaxation or diastolic asynchrony detected by color kinesis following coronary vasospasm. *Am J Cardiol* 2003; 91: 1366.
- Fukui S, Kitagawa-Sakakida S, Kawamata S, et al. Therapeutic effect of minkde on cardiac remodeling in infarcted rat hearts. *Ann Thorac Surg* 2008; 85: 562.
- Iida H, Yokoyama I, Agostini D, et al. Quantitative assessment of regional myocardial blood flow using oxygen-15-labelled water and positron emission tomography: A multicentre evaluation in Japan. *Eur J Nucl Med* 2000; 27: 192.
- Dib N, Michler RE, Pagani FD, et al. Safety and feasibility of autologous myoblast transplantation in patients with ischemic cardiomyopathy: Four-year follow-up. *Circulation* 2005; 112: 1748.
- Perin EC, Dohmann HF, Boroevic R, et al. Transendocardial, autologous bone marrow cell transplantation for severe, chronic ischemic heart failure. *Circulation* 2003; 107: 2294.
- Leor J, Aboulafia-Etzion S, Dar A, et al. Bioengineered cardiac grafts. A new approach to repair the infarcted myocardium? *Circulation* 2000; 102(suppl III): III-56.

14. Li RK, Jia ZQ, Weisel RD, et al. Survival and function of bioengineered cardiac grafts. *Circulation* 1999; 100(suppl II): II-63.
15. Suzuki K, Murtuza B, Beauchamp JR, et al. Role of interleukin-1beta in acute inflammation and graft death after cell transplantation to the heart. *Circulation* 2004; 110(11 suppl 1): II-219.
16. Tanaka H, Kawai H, Tatsumi K, et al. Relationship between regional and global left ventricular systolic and diastolic function in patients with coronary artery disease assessed by strain rate imaging. *Circ J* 2007; 71: 517.
17. Tanaka H, Kawai H, Tatsumi K, et al. Improved regional myocardial diastolic function assessed by strain rate imaging in patients with coronary artery disease undergoing percutaneous coronary intervention. *J Am Soc Echocardiogr* 2006; 19: 756.
18. Moller JE, Hillis GS, Oh JK, et al. Wall motion score index and ejection fraction for risk stratification after acute myocardial infarction. *Am Heart J* 2006; 151: 419.
19. Liu Y, Rajur K, Tolbert E, et al. Endogenous hepatocyte growth factor ameliorates chronic renal injury by activating matrix degradation pathways. *Kidney Int* 2000; 58: 2028.
20. Miyagawa S, Sawa Y, Taketani S, et al. Myocardial regeneration therapy for heart failure: Hepatocyte growth factor enhances the effect of cellular cardiomyoplasty. *Circulation* 2002; 105: 2556.
21. Taniyama Y, Morishita R, Aoki M, et al. Therapeutic angiogenesis induced by human hepatocyte growth factor gene in rat and rabbit hind-limb ischemia models: Preclinical study for treatment of peripheral arterial disease. *Gene Ther* 2001; 8: 181.
22. Li Q, Li B, Wang X, et al. Overexpression of insulin-like growth factor-1 in mice protects from myocyte death after infarction, attenuating ventricular dilation, wall stress, and cardiac hypertrophy. *J Clin Invest* 1997; 100: 1991.
23. Bock-Marquette I, Saxena A, White MD, et al. Thymosin beta4 activates integrin-linked kinase and promotes cardiac cell migration, survival and cardiac repair. *Nature* 2004; 432: 466.

e-TOCs and e-Alerts

Receive the latest developments in transplantation as soon as they're available.

Request the delivery of *Transplantation's* e-Alerts directly to your email address. This is a fast, easy, and free service to all subscribers. You will receive:

- Notice of all new issues of *Transplantation*, including the posting of new issues at the *Transplantation* website
- Complete Table of Contents for all new issues

Visit www.transplantjournal.com and click on e-Alerts.

Optimization of transmission scan duration for ^{15}O PET study with sequential dual tracer administration using N -index

Nobuyuki Kudomi · Hiroshi Watabe ·
Takuya Hayashi · Hisashi Oka · Yoshinori Miyake ·
Hidehiro Iida

Received: 14 October 2009 / Accepted: 4 March 2010 / Published online: 17 April 2010
© The Japanese Society of Nuclear Medicine 2010

Abstract

Purpose Cerebral blood flow (CBF), oxygen extraction fraction (OEF) and cerebral metabolic rate of O_2 (CMRO_2) can be quantified by PET with the administration of H_2^{15}O and $^{15}\text{O}_2$. Recently, a shortening in the duration of these measurements was achieved by the sequential administration of dual tracers of $^{15}\text{O}_2$ and H_2^{15}O with PET acquisition and integration method (DARG method). A transmission scan is generally required for correcting photon attenuation in advance of PET scan. Although the DARG method can shorten the total study duration to around 30 min, the transmission scan duration has not been optimized and has possibility to shorten its duration. Our aim of this study was to determine the optimal duration for the transmission scan. We introduced ‘ N -index’, which estimates the noise level on an image obtained by subtracting two statistically independent and physiologically equivalent images. The

relationship between noise on functional images and duration of the transmission scan was investigated by N -index.

Methods We performed phantom studies to test whether the N -index reflects the pixel noise in a PET image. We also estimated the noise level by the N -index on CBF, OEF and CMRO_2 images from DARG method in clinical patients, and investigated an optimal true count of the transmission scan.

Results We found tight correlation between pixel noise and N -index in the phantom study. By investigating relationship between the transmission scan duration and N -index value for the functional images by DARG method, we revealed that the transmission data with true counts of more than 40 Mcounts results in CBF, OEF, and CMRO_2 images of reasonable quantitative accuracy and quality.

Conclusion The present study suggests that further shortening of DARG measurement is possible by abridging the transmission scan. The N -index could be used to determine the optimal measurement condition when examining the quality of image.

N. Kudomi
Department of Medical Physics, Faculty of Medicine,
Kagawa University, Mikiyoh, Kitagun,
Kagawa 761-0793, Japan

H. Watabe (✉)
Department of Molecular Imaging in Medicine,
Osaka University Graduate School of Medicine, 2-2 Yamadaoka,
Suita, Osaka 565-0871, Japan
e-mail: watabe@mi.med.osaka-u.ac.jp

N. Kudomi · H. Watabe · T. Hayashi · H. Iida
Department of Investigative Radiology,
Advanced Medical-Engineering Center,
National Cardiovascular Center-Research Institute,
5-7-1, Fujishirodai, Suita, Osaka 565-8565, Japan

H. Oka · Y. Miyake
Department of Radiology, National Cardiovascular Center,
Hospital, 5-7-1, Fujishirodai, Suita, Osaka 565-8565, Japan

Keywords Transmission scan · PET · O-15 gas ·
Image quality

Introduction

Cerebral blood flow (CBF), oxygen extraction fraction (OEF) and cerebral metabolic rate of oxygen (CMRO_2) images have facilitated the understanding of the pathophysiological basis of cerebro-vascular disorders, and these images can be quantitatively measured using positron emission tomography (PET) with bolus administrations of ^{15}O -labeled oxygen ($^{15}\text{O}_2$) and water (H_2^{15}O) [1]. In the conventional three-step method [1–3], these functional

images were measured with separate scans for three tracers of $C^{15}O$ for cerebral blood volume (CBV), $H_2^{15}O$ for CBF and $^{15}O_2$ for $CMRO_2$, and there were additional waiting times between the scans in order to avoid the contamination of the previous tracer on the PET data. Therefore, the measurement process required a relatively long duration of around 1 h in the conventional method. Recently, the duration of the CBF, OEF and $CMRO_2$ measurements was shortened using a dual tracer autoradiography (DARG) method [4]. The DARG method is characterized by sequentially administering dual tracers of $^{15}O_2$ and $H_2^{15}O$ typically for 3 min interval during a single PET scan. When compared with the conventional three-step method, the DARG method can shorten the total study period to approximately 30 min for the set of CBV, CBF, OEF and $CMRO_2$ measurements while maintaining the image quality and quantitative accuracy.

In order to shorten the examination period even more, one option is to eliminate the CO scan which is used to correct for radioactivity in vascular space [5]. The other is to shorten the duration of the transmission scan, which is required to correct the attenuation of the number of pairs of emitted 511 keV photons in the materials of brain or other, to quantitatively estimate the radio-tracer concentrations. Usually, transmission scan is performed with external ^{68}Ge sources [6, 7]. By prolonging the duration of transmission scan, the accuracy of attenuation correction (AC) will be improved, which results in better quality and accuracy of the functional images although a patient receives additional radiation exposures. In contrast, by shortening the duration of the transmission scan, the functional images might be deteriorated due to lack of statistics. Thus, optimization of transmission scan duration is needed. Because the ^{68}Ge rod sources radioactively decay with a half-life of 270.95 days, the optimal transmission scan duration depends on the radioactivity of the ^{68}Ge source and should be determined by the true transmission scan count. To determine the optimal true count of the transmission scan, quantitative accuracy (bias) and image quality (noise on image) of the CBF, OEF and $CMRO_2$ images must be considered. The quantitative accuracy can be evaluated by comparing two images generated from different transmission scan durations. Noise equivalent counts, NEC, is often used index to evaluate noise in PET image. However, by the NEC, noise propagation from the transmission scan cannot be assessed. Alternatively, to determine the quality of images, one can perform replicated PET measurements and evaluate pixel-wise standard deviation (SD) from these images [8]. Acquiring multiple images, however, are not practical, because measurement conditions such as the administration dose and physiological state cannot be equivalent across replicated measurements.

In this study, in order to evaluate image quality, we introduced an '*N*-index' to define the noise level in an image. The validity of the *N*-index was tested using the Hoffman brain phantom [9]. In order to determine the optimal true count for the transmission scan, the introduced *N*-index was used to evaluate the noise level in the CBF, OEF and $CMRO_2$ images obtained from actual PET data with DARG method for patients with cerebro-vascular disease.

Materials and methods

Phantom studies for validation of *N*-index

It has been reported that the pixel-wise SD of a PET image reconstructed by the filtered backward projection (FBP) method was spatially uniform even in a nonhomogenous region [10]. On the basis of this suggestion, if we obtain two images of the same object with same activity concentration level from two independent scans or procedures, a spatial distribution of pixel values in the subtracted image between those two images has zero mean and its variation is related to the noise level of the images. The *N*-index is defined as the SD of the spatial distribution of the subtracted image.

To verify whether the *N*-index can be used as an index for noise level, the computed *N*-index was compared with the pixel-wise SD value of a PET image obtained from scanning a non-uniform object. We performed a PET experiment using the Hoffman brain phantom [9] filled with $^{18}F_2$ diluted in water. An ECAT EXACT HR (CTI Inc. Knoxville, USA) was used as the PET scanner, and the emission scan acquisition in the 2D mode was repeated every hour. Seven scans were performed. Before the first scan, approximately 207 MBq of $^{18}F_2$ with half-life of 109.8 min, water was injected. Each scan comprised $5 \text{ s} \times 50$ frames and the total acquired time was 250 s so that the calculated image count at each location must be almost constant across frames ($\sim 0.05\%$ change between adjacent frames and $\sim 3\%$ between the first and last frames). 72 h after the first scan (when the radioactivity of ^{18}F became negligible), two 10-min transmission scans were performed.

Two AC maps were created to correct the attenuation using the data from the two 10-min transmission scans. Using these AC maps, two dynamic images were reconstructed by employing the FBP method from the same sinogram data. Corrections for randoms, dead time, scatters, and radioactivity decay to the start time of the first scan were applied, and the Gaussian filter with a filter width of 7 mm was used. For the obtained images, we defined the *j*th pixel value as $x_{i,j}^{n,k}$ with the *k*th frame ($k = 1, 2, \dots, 50$) at *n*th scan

($n = 1, 2, \dots, 7$) with i th AC map ($i = 1, 2$). Each image had a matrix size of $128 \times 128 \times 47$ with a pixel size of $1.8 \times 1.8 \times 3.38$ mm.

The pixel-wise SD images (s_{ij}^n) were computed from all the 50 frames of the dynamic images as;

$$s_{ij}^n = \text{SD}_{k=1, \dots, 50} [x_{ij}^{n,k}] \tag{1}$$

where, $\text{SD}_{k \in K} [y_k]$ is defined as a standard deviation of y_k over K .

We calculated N -indices from two datasets to test equivalence of N -index to pixel-wise SD when amount of data change in terms of either scan duration or activity concentration as: (a) one frame data of duration 5 s and (b) 25 frames data of duration 125 s. For the dataset (a), a subtracted image ($I_j^{n,5s}$) was created by subtracting the 24th frame data with the first AC map from the 25th frame data with the second AC map as:

$$I_j^{n,5s} = x_{1j}^{n,25} - x_{2j}^{n,24} \tag{2}$$

The reason that we selected the 24th and 25th frames for the subtraction was to minimize the influence of physical decay in the pixel value. For the dataset (b), even-numbered frames with the first AC map and odd-numbered frames with the second AC map were summed in order to obtain two independent (but must be identical in terms of the radioactivity count at each location) images. By subtracting the two images, the subtracted image was created as:

$$I_j^{n,125s} = \frac{1}{25} \sum_{k \in \text{odd}} x_{1j}^{n,k} - \frac{1}{25} \sum_{k \in \text{even}} x_{2j}^{n,k} \tag{3}$$

The reason that we summed the frames alternately was to minimize the influence of physical decay in the pixel value. The subtracted image has a mean value that is approximately and uniformly zero.

A circular region of interest (ROI) (10.7 cm in diameter, 3620 pixels) was placed in the brain region on a slice at the level of thalamus. The mean SD value (M_{SD}^n) of s_{ij}^n and the N -index ($NI^{n,t}$) of $I_j^{n,t}$ inside the ROI were calculated and compared.

Subjects and PET procedure

For the CBF and CMRO₂ measurements, we performed a series of PET scans on six human subjects with cerebrovascular disease ($n = 6$, age = 69 ± 3 years, body weight = 64 ± 4 kg). The DARG approach [4, 11] was employed to compute the CBF and CMRO₂ images. An ECAT EXACT 47 (CTI Inc. Knoxville, USA), equipped with three rotating ⁶⁸Ge-⁶⁸Ga rod sources was used as the PET scanner. The PET procedures were approved by the ethics committee of the National Cardiovascular Center.

Transmission scans with multiple frames ($60 \text{ s} \times 9 \text{ frames}$ and $30 \text{ s} \times 2 \text{ frames}$) were performed for 10 min. After the transmission scan, a 4-min static emission scan along with C¹⁵O administration was performed. Subsequently, a dynamic DARG H₂¹⁵O-¹⁵O₂ scan [4] was started with the sequential administration of gaseous ¹⁵O₂ (3000 MBq, 1-min inhalation) followed by H₂¹⁵O (1110 MBq, intra-venous injection into the right brachial vein) administration after 6 min. The DARG scan sequence comprised 10 s × 6 frames, 20 s × 6 frames, 30 s × 4 frames, 10 s × 4 frames, 5 s × 10 frames and 15 s × 2 frames. All data were acquired in the 2D mode with extended septa.

To obtain the arterial input function, a catheter was inserted into the brachial artery, and blood was withdrawn at a flow rate of 4 ml/min during each emission PET scan. The arterial blood time activity curve (TAC) was continuously monitored using a GSO input function monitor [12].

Data processing

From the multi-frame transmission data with 11 frames, two sets for 30, 60, 120, 180, 240 and 300 s were generated by adding the frames and avoiding duplications. In addition, the sum of the transmission data with a duration of 600 s was obtained. On the basis of the obtained transmission data and the blank scan data, 13 AC maps were generated defined as AC_{*i*}^{*t*}, where $i = 1, 2$ (index of the sets), and $t = 30, 60, 120, 180, 240, 300$ s (transmission data time duration) and AC₁^{600s}.

Along with detector normalization, the static images for the C¹⁵O scan and the dynamic image for the ¹⁵O₂-H₂¹⁵O emission scan sinograms were corrected for dead time and radioactive decay in each frame. Tomographic images were reconstructed using these corrected sinograms obtained by the FBP method with 7-mm Gaussian filtering. AC was applied to the C¹⁵O static image using the AC map obtained from the 600-s transmission data, (i.e., AC₁^{600s}), and to the ¹⁵O₂-H₂¹⁵O dynamic image using all the generated AC map data of AC_{*i*}^{*t*}. Thus, 13 dynamic images were obtained. The pixel value was defined as $x_{ij}^k(i,t)$ for j th pixel value with k th frame using AC_{*i*}^{*t*}. A scatter correction was also applied. The reconstructed dynamic images had a matrix size $128 \times 128 \times 47$ with a pixel size of $1.8 \times 1.8 \times 3.38$ mm.

The following three steps were employed to sum up a part of the reconstructed dynamic image for the ¹⁵O₂-H₂¹⁵O scan during each oxygen (180 s from the start of oxygen inhalation, indicated as: $k \in \text{O}_2$) and water (120 s from the increase in the brain tissue TAC, indicated as: $k \in \text{H}_2\text{O}$) phase. First, all the frames were summed as: $\sum_{j \in (1,t)}^k x_{ij}^k$ and $\sum_{k \in \text{H}_2\text{O, all}}^k x_{ij}^k$. Second, all the even-numbered frames

were summed as: $\sum^{k \in O_2, \text{even}} x_{j,(2,t)}^k$ and $\sum^{k \in H_2O, \text{even}} x_{j,(2,t)}^k$. Lastly, all the odd-numbered frames were summed as: $\sum^{k \in O_2, \text{odd}} x_{j,(1,t)}^k$ and $\sum^{k \in H_2O, \text{odd}} x_{j,(1,t)}^k$. We assumed two images summed with even- and odd-numbered frames are physiologically and quantitatively equivalent and statistically independent.

Arterial blood TACs were corrected for radioactivity decay and dispersion ($\tau = 4$ s) [4, 13, 14] and delay [3, 4, 15] further, the $^{15}O_2$ and $H_2^{15}O$ contents were separated [11]. The obtained $^{15}O_2$ and $H_2^{15}O$ arterial TACs were used as the water and oxygen input functions as $A_w(t)$ and $A_o(t)$, respectively.

Sets of CBF, OEF and $CMRO_2$ images were generated using the DARG approach as described previously [4] by using a set of summed images in both the oxygen and water phases ($\sum^{k \in O_2, \rho} x_{j,(1,t)}^k$ and $\sum^{k \in H_2O, \rho} x_{j,(1,t)}^k$, where ρ indicates the rule of sum, i.e., all, even or odd), $^{15}O_2$ and $H_2^{15}O$ input functions $A_w(t)$ and $A_o(t)$ and cerebral blood volume (CBV) image that was obtained from the $C^{15}O$ scan data [3, 4]. This procedure was repeated for all sets of images and the functional images for j th pixel were obtained as: $CBF_{j,(i,t)}^\rho$, $OEF_{j,(i,t)}^\rho$ and $CMRO_{2j,(i,t)}^\rho$, where indices (i, t) are same as those for AC, and ρ is the rule of sum.

Dependency of quantitative CBF/OEF/ $CMRO_2$ accuracy on the transmission true counts

An ROI was placed on the frontal, temporal and parietal cortical region (5000–10000 pixels) of the image and the CBF, OEF and $CMRO_2$ values were extracted from all the datasets. The mean of these extracted values was expressed as the percent difference between the values obtained from the functional images computed with AC_1^i and with AC_1^{600s} for all datasets obtained from the emission data as:

$$\frac{R[\text{Func}_{j,(1,t)}^{\text{all}}] - R[\text{Func}_{j,(1,600s)}^{\text{all}}]}{R[\text{Func}_{j,(1,600s)}^{\text{all}}]} \times 100\% \tag{4}$$

where R indicates mean pixel value inside the ROI and Func indicates either CBF, OEF or $CMRO_2$.

Dependency of CBF/OEF/ $CMRO_2$ image quality on the transmission true counts

Subtracted images were created by subtracting the functional images between even- and odd-numbered frames as:

$$I_{j,t}^{\text{Func}} = \text{Func}_{j,(1,t)}^{\text{even}} - \text{Func}_{j,(2,t)}^{\text{odd}} \tag{5}$$

for the j th pixel. The N -index in the ROI, placed on the frontal, temporal and parietal cortical region as above, for these subtracted images were calculated as:

$$NI_{\text{Func}} = SD_{j \in \text{ROI}} [I_{j,t}^{\text{Func}}] \tag{6}$$

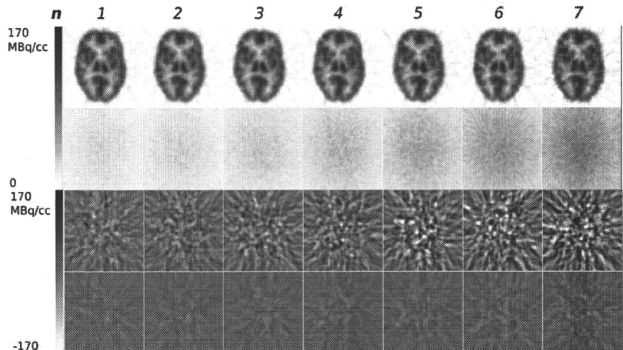
The obtained N -indices were expressed as a function of the total true count of the transmission scan data.

Results

Phantom studies for validation of N -index

Figure 1 shows representative slices of the obtained images of mean, SD, and subtraction. The later scan has more noise due to count statistics, which can be observed in SD image and the subtracted images in Fig. 1. Despite the difference in the activity distribution, the SD image was almost uniform. The relationship between the mean value of the SD image (M_{SD}) and N -index (NI) in the same ROI

Fig. 1 Representative slices of the reconstructed images obtained from the phantom studies. The first row is averaged image, the second row is SD image, the third row is the subtracted image for the dataset (a), and the fourth row is the subtracted image for the dataset (b). Each column corresponds the images from n th scan (total seven scans)



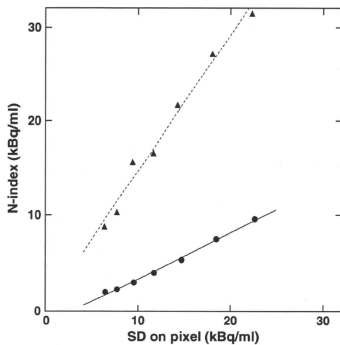


Fig. 2 The relationship between the mean SD value and N -index obtained from the subtracted image with the same ROI region of the brain phantom. The regression line was expressed as $y = 1.44x - 0.331$ (kBq/ml) ($r = 0.99$, $n = 7$), and $y = 0.47x - 1.29$ (kBq/ml) ($r = 0.99$, $n = 7$), for 5 s (closed triangle) and 125 s (closed circle) in calculating N -index, respectively

is shown in Fig. 2. The regression line is expressed as $NI = 1.44M_{SD} - 0.331$ (kBq/ml) ($r = 0.99$) and $NI = 0.47M_{SD} - 1.285$ (kBq/ml) ($r = 0.99$), where r is correlation coefficient, for the subtracted images obtained from the 5- and 125-s data, respectively. The results shown in Figs. 1 and 2 support the assumption that the SD of the pixel value is uniform in a non-homogeneous image that was reconstructed using the FBP method. Furthermore, the present N -index was correlated with the SD and could be employed to compare the image qualities.

Dependency of quantitative CBF/OEF/CMRO₂ accuracy on the transmission true counts

Figure 3 shows the percent difference in the CBF (a), OEF (b) and CMRO₂ (c) values when compared with those computed using the 10-min AC map. The results show that the quantitative values obtained during the CBF, OEF and CMRO₂ measurements are almost identical, namely, difference was <5% to those obtained when AC was performed using the transmission data containing true counts more than 40 Mcounts.

Dependency of the CBF/OEF/CMRO₂ image quality on the transmission true counts

Figure 4 shows the N -indices in the CBF (a), OEF (b) and CMRO₂ (c) images, as a function of the number of true counts of the transmission data. The present results show that the qualities of the CBF, OEF and CMRO₂ images

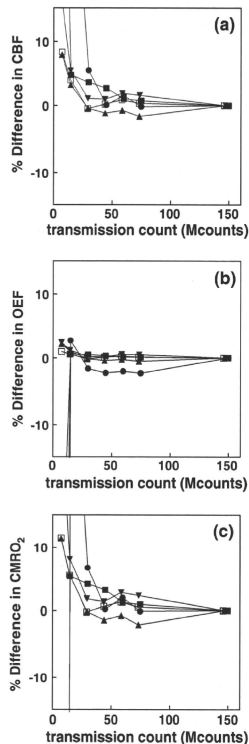


Fig. 3 Percent difference in the CBF, OEF and CMRO₂ values when compared with those obtained from the 10-min transmission data, as a function of the true counts of the transmission data. Each type of symbol corresponds to each subject ($n = 6$). The indicated values were extracted from the ROI in the frontal, parietal and temporal cortex regions

were almost equal to those in which the true counts of the transmission data used exceeded 40 Mcounts.

Discussion and conclusion

Our purpose of this study was to shorten the transmission scan duration for ¹⁵OPET study with DARG measurement. By evaluating bias and noise on the functional images of the CBF, OEF and CMRO₂ due to noise in transmission data, optimal transmission true count in DARG measurement was

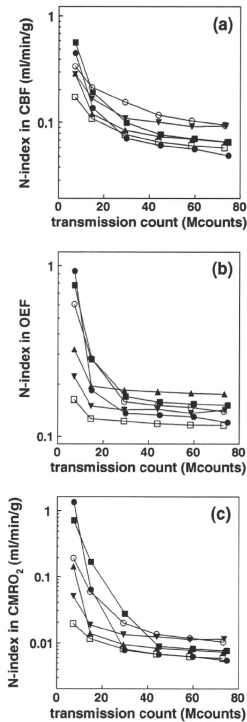


Fig. 4 The N -indices for the CBF, OEF and $CMRO_2$ images that were obtained from various true counts of the transmission data as a function of the true counts of the transmission data. Each type of symbol corresponds to each subject ($n = 6$). The symbols used and ROI are the same as that used for Fig. 3

determined. We found 40 Mcounts of the true count in the transmission scan was optimal, and consequently, we were able to shorten the total duration of the DARG examination.

We introduced the N -index to compare the noise level on inhomogeneous functional images. The benefit of using N -index is that by one index number, one can characterize the noise in functional image derived from PET data and DARG measurement which have complex noise propagations from several error sources. The validity of the N -index was tested in the phantom study. We found tight correlation between pixel noise and the N -index.

The present result using the brain phantom supported the assumption that the SD of a pixel value was spatially

uniform even in a non-homogeneous region of an FBP reconstructed image (Fig. 1). Furthermore, the regression line between the SD value from the statistically obtained SD image and the N -index from the subtracted image for 5- and 125-s data were highly correlated ($r = 0.99$) (Fig. 2). The slope for 5-s data was approximately $\sqrt{2}$, where the SD of the image obtained by subtraction of two 5-s data (statistically corresponding to 10 s) could be expected to be $\sqrt{2}$ greater than that of the original image. For 125-s data, 1/5 of statistical noise compared to 5-s data is expected. However, N -index for 125-s data overestimated in 18% in average than expected. One possible reason of this overestimation is influence of inhomogeneity of the reconstructed image. Therefore, the N -index cannot be used to estimate absolute noise level in the image, but the N -index is still valid for study which compares relative noise levels among multiple images.

Using the N -index, we examined the change of image quality in the CBF, OEF and $CMRO_2$ as the noise level based on the change in the true counts of the transmission data. One of the advantages using the N -index is that it allows us to compare the noise level of non-uniform images such as that of the brain, using the data obtained by ordinal PET scan procedure. In order to investigate the noise level of the PET images using parameters other than the N -index, the PET scans must be replicated for a human subject. However, this appears unlikely due to the excessive radiation dose that would need to be administered to the subject. Furthermore, it might be quite hard to maintain the equivalent measurement conditions such as the radiation dose, as well as the physiological conditions of the subjects.

In this study, two implicit conditions were assumed: the SD on pixel value is uniform for the targeted region and odd- and even-numbered frames have the same statistical properties. The condition of uniform distribution of the SD on the functional image might not be microscopically fulfilled due to nature of nonlinearity of DARG method. However, in global, noise on the reconstructed image could be linearly propagated to the functional image and we considered this assumption was valid for computing the N -index. The N -index can be applied to other cases such as a variety of tracers and organs in order to examine the image quality as far as those conditions are satisfied. It should be noted that the CBF and $CMRO_2$ parametric images are required to be assessed quantitatively [16], thus the present study was validated with images reconstructed by FBP method. Limitation of the present method is that the N -index may not be applied to images such as those reconstructed by the maximum likelihood expectation maximization based algorithm, because the uniformity of SD across pixels is not guaranteed. However, a similar procedure of the present method still has possibility to be

applied, if, for example, coefficient of variation is uniform across pixels.

When N -index was estimated from two images with either emission or transmission data being common, the variation on image can be calculated as a sum of each variation and subtraction of covariance, canceling effect of noise from common data. Consequently, the N -index only reflects noise on either transmission or emission data. Thus, we estimated N -index by subtracting fully independent images. The validity of N -index could be tested in the phantom study using common transmission data; however, we still computed N -index using fully independent images, because the test should be done in the same conditions as the experimental study.

The present results showed that poor count statistics in transmission scanning resulted in significant bias in quantitative values of CBF, OEF and CMRO₂. As has been mathematically described [17], AC factor, i.e. blank/transmission is biased by factor of $(1 + 1/m)$, where m is a transmission count on a corresponding pixel. Therefore, the poorer the transmission scan count is, the higher the AC factor becomes. In view of image quality, noise in transmission data influences functional image as shown in Fig. 4. On the other hand, as indicated in Fig. 4, extra longer transmission scan gains no statistical benefit. The optimized transmission scan duration will be determined by relative noise level of the transmission data against the emission data.

In this paper, we used fixed duration of 600 s of the transmission scan for CO image, assuming little effect of noise on CO image. One reason for this assumption is that 50% error in CBV value derives around only 3% error in OEF and CMRO₂ images [4], suggesting 50% noise on CBV image resulting only 3% noise on OEF and CMRO₂ images. As shown in Fig. 4, the degree of noise on the OEF and CMRO₂ images are around 20–25%, and the level of noise is quite high compared to level of noise from CBV image.

Motion of subject, during a scan, could be a problem to calculate N -index. However, movement of a subject during a scan affects both the odd-and even-numbered frames simultaneously, and thus the statistical properties between two summed images will stay the same. Thus, motion of a subject during a scan might not be that critical with regards to the N -index, as far as the motion does not deteriorate the image used to assess the function of the targeted organ.

The comparison of the N -indices between subjects or between different functional images cannot be performed because the N -indices offer information of relative noise level but not absolute noise. Thus, a meaningful comparison can be made between images of the same subject and of the same cerebral function (such as CBF and CMRO₂).

It is generally accepted that accurate ACs require transmission scanning using external sources [6, 7], although there are excellent techniques designed to shorten or eliminate the transmission scan duration, such as the transmission-data-based segmented method for the AC map [18, 19] or the emission-based AC map calculation [20]. The present approach might be applicable to investigate the noise level in segmented or emission-based methods, which should enable us to further shorten the duration of a PET examination.

Boellaard et al. demonstrated the relationship between the transmission scan counts and phantom diameter, and they found that this relationship did not restrict the application of the count-based transmission scans for correcting the reduction in the rod source strength [21]. However, they indicated that when the subject is extremely small, a transmission scan based on an acquired number of true counts should not be applied. This is because the counts for lines of response not passing through the subject would increase. Further studies are required to determine the optimal examination conditions for such situations.

We found that the true counts of the transmission data exceeding 40 millions (corresponds to 3 min scan in this study) were appropriate for the CBF, OEF and CMRO₂ measurement by DARG method in terms of both quantitative accuracy and image quality, consequently we can shorten the examination duration for obtaining those images. Conventional DARG measurement in clinical study uses 10 min of transmission scan, while 9 min of emission scan of dual tracers of ¹⁵O₂ and H₂¹⁵O, in addition to 4 min of C¹⁵O scan [22]. If one can shorten the transmission scan to 3 min, total scan duration is 16 min (30% reduction). Currently, another C¹⁵O scan for CBV correction with regards to the assessment of CBF, OEF and CMRO₂ is still required, an additional mathematical formulation strategy, like the basis function method [23] could eliminate this requirement [5].

In conclusion, we determined the required transmission true count that maintains the quantitative accuracy and image quality for PET studies with H₂¹⁵O and ¹⁵O₂. According to our results, the total study duration could be minimized by shortening the transmission scan. Although the obtained results in the present study were measurement condition specific, the N -index could be used to determine PET scanning procedures.

Acknowledgments The authors would like to thank Ms Atradakani for her invaluable help on preparing this article. The authors gratefully acknowledge the staff of the Department of Nuclear Medicine, Hospital and the Department of Investigative Radiology, Research Institute, National Cardiovascular Center. The present work was supported by the Program for Promotion of Fundamental Studies in Health Science of the Organization for Pharmaceuticals and

Medical Devices Agency of Japan (PMDA), and the Nakatani Electronic Measuring Technology Association of Japan, and by the Ministry of Education, Science, Sports and Culture, Grant-in-Aid for Young Scientists (start-up), 21890171, 2009.

References

- Mintun M, Raichle M, Martin W, Herscovitch P. Brain oxygen utilization measured with O-15 radiotracers and positron emission tomography. *J Nucl Med*. 1984;25:177–87.
- Hatazawa J, Fujita H, Kanno I, Satoh T, Iida H, Miura S, et al. Regional cerebral blood flow, blood volume, oxygen extraction fraction, and oxygen utilization rate in normal volunteers measured by the autoradiographic technique and the single breath inhalation method. *Ann Nucl Med*. 1995;9:15–21.
- Shidahara M, Watabe H, Kim K, Oka H, Sago M, Hayashi T, et al. Evaluation of a commercial PET tomograph-based system for the quantitative assessment of rCBF, rOEF and rCMRO2 by using sequential administration of 15O-labeled compounds. *Ann Nucl Med*. 2002;16:317–27.
- Kudomi N, Hayashi T, Teramoto N, Watabe H, Kawachi N, Ohta Y, et al. Rapid quantitative measurement of CMRO(2) and CBF by dual administration of (15O)-labeled oxygen and water during a single PET scan—a validation study and error analysis in anesthetized monkeys. *J Cereb Blood Flow Metab*. 2005;25:1209–24.
- Kudomi N, Hayashi T, Watabe H, Iida H. Rapid CBF/CMRO₂ measurement in a single PET scan with dual tracer administration. *J Cereb Blood Flow Metab*. 2005;25:S672.
- Bailey D. Transmission scanning in emission tomography. *Eur J Nucl Med*. 1998;25:774–87.
- Ostertag H, Kbler W, Doll J, Lorenz W. Measured attenuation correction methods. *Eur J Nucl Med*. 1989;15:722–6.
- Watabe H, Matsumoto K, Senda M, Iida HP. Performance of list mode data acquisition with ECAT EXACT HR and ECAT EXACT HR + positron emission scanners. *Ann Nucl Med*. 2006;20:189–94.
- Hoffman E, Cutler P, Digby W, Mazziotta J. 3-D phantom to simulate cerebral blood flow and metabolic images for PET. *IEEE Trans Nucl Sci*. 1990;37:616–20.
- Pajevic S, Daube-Witherspoon M, Bacharach S, Carson R. Noise characteristics of 3-D and 2-D PET images. *IEEE Trans Med Imaging*. 1998;17:9–23.
- Kudomi N, Watabe H, Hayashi T, Iida H. Separation of input function for rapid measurement of quantitative CMRO₂ and CBF in a single PET scan with a dual tracer administration method. *Phys Med Biol*. 2007;52:1893–908.
- Kudomi N, Choi E, Yamamoto S, Watabe H, Kim K, Shidahara M, et al. Development of a GSO detector assembly for a continuous blood sampling system. *IEEE Trans Nucl Sci*. 2003;50:70–3.
- Iida H, Kanno I, Miura S, Murakami M, Takahashi K, Uemura K. Error analysis of a quantitative cerebral blood flow measurement using H₂(15)O autoradiography and positron emission tomography, with respect to the dispersion of the input function. *J Cereb Blood Flow Metab*. 1986;6:536–45.
- Lammertsma A, Cunningham V, Deiber M, Heather J, Bloomfield P, Nutt J, et al. Combination of dynamic and integral methods for generating reproducible functional CBF images. *J Cereb Blood Flow Metab*. 1990;10:675–86.
- Iida H, Higano S, Tomura N, Shishido F, Kanno I, Miura S, et al. Evaluation of regional differences of tracer appearance time in cerebral tissues using [15O] water and dynamic positron emission tomography. *J Cereb Blood Flow Metab*. 1988;8:285–8.
- Ibaraki M, Miura S, Shimosegawa E, Sugawara S, Mizuta T, Ishikawa A, et al. Quantification of cerebral blood flow and oxygen metabolism with 3-dimensional PET and 15O: validation by comparison with 2-dimensional PET. *J Nucl Med*. 2007;49:50–9.
- Freedman N, Bacharach S, Carson R, Price J, Dilisizian V. Effect of smoothing during transmission processing on quantitative cardiac PET scans. *J Nucl Med*. 1996;37:690–4.
- Xu M, Luk W, Cutler P, Digby W. Local threshold for segmented attenuation correction of PET imaging of the thorax. *IEEE Trans Nucl Sci*. 1994;41:1532–7.
- Xu M, Cutler P, Luk W. Adaptive, segmented attenuation correction for whole-body PET imaging. *IEEE Trans Nucl Sci*. 1996;43:331–6.
- Weinzapfel B, Hutchins G. Automated PET attenuation correction model for functional brain imaging. *J Nucl Med*. 2001;42:483–91.
- Boellaard R, Lingem Av, Balen Sv, Lammertsma A. Optimization of attenuation correction for positron emission tomography studies of thorax and pelvis using count-based transmission scans. *Phys Med Biol*. 2004;49:N31–8.
- Iwanishi K, Watabe H, Hayashi T, Miyake Y, Minato K, Iida H. Influence of residual oxygen-15-labeled carbon monoxide radioactivity on cerebral blood flow and oxygen extraction fraction in a dual-tracer autoradiographic method. *Ann Nucl Med*. 2009;23:363–71.
- Gunn R, Lammertsma A, Hume S, Cunningham V. Parametric imaging of ligand receptor binding in PET using a simplified reference region model. *Neuroimage*. 1997;6:279–87.

Multicenter Evaluation of a Standardized Protocol for Rest and Acetazolamide Cerebral Blood Flow Assessment Using a Quantitative SPECT Reconstruction Program and Split-Dose ^{123}I -Iodoamphetamine

Hidehiro Iida^{1,2}, Yoji Nakagawara^{1,3}, Kohei Hayashida^{1,4}, Kazuhito Fukushima^{1,5}, Hiroshi Watabe^{1,2}, Kazuhiro Koshino^{1,2}, Tsutomu Zeniya^{1,2}, and Stefan Eberl^{1,6}

¹Dual-Table Autoradiography SPECT Research Group in Japan, Osaka, Japan; ²National Cerebral and Cardiovascular Center—Research Institute, Osaka, Japan; ³Nakamura Memorial Hospital, Sapporo, Japan; ⁴Takeda Hospital, Kyoto, Japan; ⁵National Cerebral and Cardiovascular Center—Hospital, Osaka, Japan; and ⁶Royal Prince Alfred Hospital, Sydney, Australia

SPECT can provide valuable diagnostic and treatment response information in large-scale multicenter clinical trials. However, SPECT has been limited in providing consistent quantitative functional parametric values across the centers, largely because of a lack of standardized procedures to correct for attenuation and scatter. Recently, a novel software package has been developed to reconstruct quantitative SPECT images and assess cerebral blood flow (CBF) at rest and after acetazolamide challenge from a single SPECT session. This study was aimed at validating this technique at different institutions with a variety of SPECT devices and imaging protocols. **Methods:** Twelve participating institutions obtained a series of SPECT scans on physical phantoms and clinical patients. The phantom experiments included the assessment of septal penetration for each collimator used and of the accuracy of the reconstructed images. Clinical studies were divided into 3 protocols, including intrainstitutional reproducibility, a comparison with PET, and rest–rest study consistency. The results from 46 successful studies were analyzed. **Results:** Activity concentration estimation (Bq/mL) in the reconstructed SPECT images of a uniform cylindrical phantom showed an interinstitution variation of $\pm 5.1\%$, with a systematic underestimation of concentration by 12.5%. CBF values were reproducible both at rest and after acetazolamide on the basis of repeated studies in the same patient (mean \pm SD difference, -0.4 ± 5.2 mL/min/100 g, $n = 44$). CBF values were also consistent with those determined using PET (-6.1 ± 5.1 mL/min/100 g, $n = 6$). **Conclusion:** This study demonstrates that SPECT can quantitatively provide physiologic functional images of rest and acetazolamide challenge CBF, using a quantitative reconstruction software package.

Key Words: ^{123}I -iodoamphetamine; cerebral blood flow; acetazolamide; SPECT; vascular reactivity; quantitation

J Nucl Med 2010; 51:1624–1631

DOI: 10.2967/jnumed.110.078352

Current clinical practice using SPECT relies largely on interpretation of qualitative images reflecting physiologic function. Quantitative functional parametric images may be obtained by applying mathematic modeling to SPECT data corrected for attenuation and scatter. Quantitative regional cerebral blood flow (CBF) (*1–3*) and cerebral vascular reactivity (CVR) in response to acetazolamide challenge (*4–6*) have been obtained with these techniques. One major application of such quantitative SPECT (QSPECT) approaches is the evaluation of ischemic status in patients with occlusion or stenosis in their middle cerebral arteries, to provide prognostic information of the outcome of revascularization therapies (*7*). Quantitative analysis in SPECT has also been demonstrated in the assessment of binding potential for several neuroreceptor ligands (*8,9*), for the quantitative assessment of regional myocardial perfusion (*10,11*), and for the assessment of radio-aerosol deposition and clearance in healthy and diseased lungs (*12*). However, providing the standardized quantitative approach required for multicenter clinical trials has so far received only limited attention. Challenges remain in providing consistent quantitative data across institutions using a variety of SPECT equipment and vendor-specific reconstruction strategies (*13*). This limitation is attributed to a lack of standardized procedures in the reconstruction software offered by vendors, particularly in terms of correcting attenuation and scatter. Kinetic modeling for physiologic parameter estimation is also not part of the vendors' standard SPECT software. Although separate packages can be purchased for this purpose, they are not integrated and are flexible general-purpose packages, requiring considerable skill and knowledge to effectively use. Thus, they are not ideal for routine clinical use.

Scatter and attenuation occur in the object and are thus object-dependent but are not dependent on the geometry of the imaging equipment (*14*). Therefore, once a software program is developed to provide accurate image reconstruction with compensation for both attenuation and scatter, the

Received Apr. 27, 2010; revision accepted Jul. 14, 2010.

For correspondence or reprints contact: Hidehiro Iida, Department of Investigative Radiology, National Cerebral and Cardiovascular Center—Research Institute, 5-7-1 Suita City, Osaka 565-0855, Japan.

E-mail: iida@n.cvc.go.jp

COPYRIGHT © 2010 by the Society of Nuclear Medicine, Inc.